A Static FEA Framework for Fast Analysis of HTS Armature Windings in AC Superconducting SMPM Machines

Christian Hartmann, *Member, IEEE*, Runar Mellerud, *Student Member, IEEE*, Jonas Kristiansen Nøland, *Senior Member, IEEE*, and Robert Nilssen

***Abstract*—Macroscopic superconductivity models have improved significantly over the last decades. Formulations and methods have been developed to faster solve problems involving high-temperature superconductors (HTS). Despite these developments, finite element analysis (FEA) of AC superconducting machines (SCMs) with HTS coils still remains time-consuming. The combined burden from the HTS models and the moving mesh makes the models complex and slow. To deal with this challenge, a new framework for FEA of AC SCMs with surface-mounted permanent magnet (SMPM) rotors and HTS armature windings is proposed in this paper. In this approach, the rotating rotor geometry is emulated with a stationary array of small PM segments excited with time-varying boundary sources. The major benefit of this approach is that the models can be realized without moving meshes, which increases the computation speed by more than one order of magnitude. In our dedicated case study of a complete SCM design, the speedup factors are 17.0x and 37.9x for the mixed H-A and T-A formulations, respectively. Over a large parametric space of 22 design permutations, the highest relative error in calculated HTS loss was 4.12 percent. As a result, this work enables the designer to perform much more comprehensive performance studies of SCMs.**

***Index Terms*—High-temperature superconductors, HTS, H-A formulation, T-A formulation, superconducting electric machines, FEA, FEM.**

I. Introduction

THE mixed H-A [1] and T-A [2] formulations are widely used for performing finite element analysis (FEA) of rotating electric machinery with high-temperature superconductors (HTS) [3], [4]. Both mixed formulations enable macroscopic modeling of the HTS material by employing the E-J power-law [5] to describe the effective resistivity of the superconducting (SC) layer in the HTS.

Henceforth, the mixed H-A and the mixed T-A formulations are referred to simply as the H-A formulation and the T-A formulation, respectively.

Manuscript submitted December 23, 2022. Revised April 5, 2023. This work was supported in part by the Research Council of Norway (RCN) under Grant 259860 (Doctoral Scholarship). (*Corresponding author: Christian Hartmann*.)

Christian Hartmann is with the Institute for Energy Technology (IFE), 1777 Halden, Norway, and also with the Department of Electric Power Engineering, Norwegian University of Science and Technology (NTNU), 7034 Trondheim, Norway (e-mail: christian.hartmann@ife.no).

Runar Mellerud, Jonas Kristiansen Nøland, and Robert Nilssen are with the Department of Electric Power Engineering, Norwegian University of Science and Technology (NTNU), 7034 Trondheim, Norway (e-mail: runar.mellerud@ntnu.no; jonas.k.noland@ntnu.no; robert.nilssen@ntnu.no).

Over the course of the last two decades, significant achievements have been made to make HTS models compute faster. Notable here is the introduction of the T-A formulation [2], which in most cases outperforms the H and H-A formulations in terms of computational speed [6]. Techniques to reduce the level of details in coil models while retaining acceptable accuracy, such as multi-scale and homogenized models [6], have also contributed to faster FEA. In addition to these modeling techniques, studies on the influence of element order, solver settings, and so on [7]–[9] have also provided valuable insight into how the trade-off between computation speed and accuracy can be optimized. With these advancements, together with a steady improvement in computer performance, simulations of detailed HTS coil models can be run in the order of minutes, provided that they are surrounded by simple geometries. However, it is more demanding when the HTS coils are placed in the stator of an AC superconducting electric machine (SCM).

In modern FEA software, such as COMSOL Multiphysics, a rotating electric machine model consists of a static and a rotating mesh, with a sliding boundary between the two [3]. The calculations are then performed in time steps. This approach to modeling electric machines has several advantages. The models are flexible in use and yield accurate results. The downside to this approach is that the models can become computationally demanding, especially for SCMs with HTS armature windings. The combined burden from the rotating mesh and the HTS models drives up the computation times. The resulting FEA models can also be prone to convergence problems which makes it necessary to tighten the solver parameters. As a result, the time it takes to run a single simulation of an SCM model is commonly in the order of hours [10]. This effectively disqualifies the use of the FEA models for larger parametric studies where numerous combinations of slot and HTS coil geometries are to be investigated, often in combination with different material options.

This paper presents a highly efficient method for speeding up the FEA of AC superconducting machines with surface-mounted permanent magnets (PM) in the rotor and HTS armature windings in the stator. Instead of focusing on improving the macroscopic HTS models, the method addresses the need to reduce the complexity of the machine's air gap model. The moving mesh is replaced by a mesh that remains completely static over all simulated time-steps. The essence of the proposed method is to replace the actual PM configuration

on the rotor with an array of small, discretely magnetized PM segments distributed along the rotor circumference (*small-segment* representation). The relative movement between the rotor and the stator is emulated by applying individual time-varying excitation sources on each of these small PM segments. As will be shown, the absence of a rotating mesh in the FEA model speeds up the calculations by at least one order of magnitude. The method is especially suited for larger parametric or optimization studies of stator and slot design in SMPM machines with HTS coils, where HTS AC loss prediction is of key importance. Since the actual PM geometry is sacrificed in this framework, the method is not suited for rotor optimization. However, supplementary studies of rotor phenomena can be performed on models where the HTS coils are replaced by conventional conductors, which significantly reduce computation times.

The framework proposed in this paper has commonalities with the work of Tessarolo *et al.* [11], especially the small-segment approach. However, the methodology devised by Tessarolo *et al.* [11], [12] is specifically developed for conventional armature coils. It utilizes a time-harmonic FEA (TH-FEA) and uses superposition to sum loss contributions from the different time-harmonics. This approach is not applicable to problems involving HTS models due to the magnetic history-dependency [13] and the highly non-linear resistivity in the HTS. To overcome these limitations, we have developed a methodology that works with time-stepping FEA. It is especially suitable for SCMs, where it models the interaction between the HTS coils and the rotor field with high accuracy, in addition to being much faster than rotating models.

There are several other effective methods, such as those proposed by Meeker [14] and Hughes [15], available to address the challenge of remeshing in FEA. Which method is best suited will depend on several factors, such as the objective of the study and the skills of the designer. The framework proposed in this paper is characterized by its ease of implementation as the static representation is established through the FEA model's geometry and boundary conditions. It also works readily with the H-A and T-A formulations.

The FEA environment of COMSOL Multiphysics v. 5.6 and the IDUN cluster computing facilities [16] at NTNU have been used to carry out the work herein. All models investigated have been implemented in both the H-A and T-A formulations. The SCM geometry and parametric variations in this study are also tailored to expose the HTS coils to a range of different operating conditions. This has been done to give a broad basis for comparing the performance of the small-segment representation with conventionally modeled rotor PMs.

The paper is organized as follows. In Section II, we present the SCM, which will be used to demonstrate the small-segment representation. Next, the methodology is described in Section III. This method is then applied to the studied SCM in Section IV. Lastly, the performance of the small-segment representation is compared to FEA models with Halbach array rotors in Section V. This comparison is performed over three different parametric studies using both the H-A and T-A formulations. Section VI contains supplementary results from more detailed coil models. Finally, Section VII concludes the paper while Appendix A provides additional information to the detailed simulation results.

II. Selected SCM Case Study

The proposed methodology is demonstrated on a ten-pole double-layer concentrated winding machine with HTS windings in the stator and a four-segment Halbach array without a back-iron in the rotor. The SCMs two-dimensional (2D) geometry is depicted in Fig. 1, where the anti-symmetry line is indicated. It allows for FEA of a half-machine segment of the SCM.

The studied SCM is based on a proposed design for a $2.5\,\mathrm{MW}$ SCM for aircraft propulsion [17]. The slot shape has been altered to make the HTS coils more exposed to the rotor field and, thereby, more sensitive to any potential inaccuracies stemming from the small-segment representation. The dimensions of the armature coils have also been shrunk to allow for movement and rotation of the coils without colliding with adjoining parts since the original coil height in reference [17] is too large for some of the parametric study cases conducted in Section V. The smaller coils lead to a derating of the machine to approximately $1\,\mathrm{MW}$. Its specifications are listed in Table I.

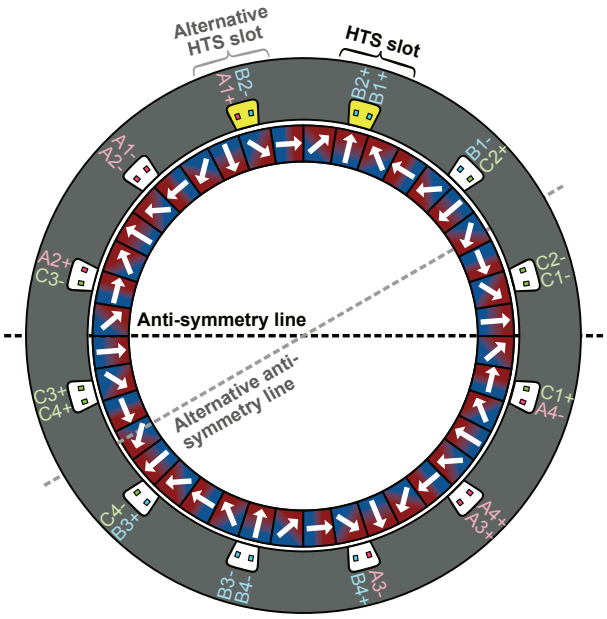

Fig. 1. 2D model of the of the studied SCM configured with a PM rotor arranged as a Halbach array. Only one of the 12 stator slots contains HTS models (i.e., the "HTS slot") while the other slots are modeled with lossless conductors. By shifting the angle of the anti-symmetry line it is possible to position different phase combinations in the HTS slot. This is further explained in Fig. 3 and Section IV-C.

III. Description of Methodology

Although the studied SCM in Fig. 1 has rotor PMs arranged in a Halbach array, the methodology described herein is generally applicable to any SCM with surface-mounted PMs in the rotor. It can apply to other rotor topologies as well, but one important limitation is that the framework developed here does not model rotating magnetic saliency. In certain designs,

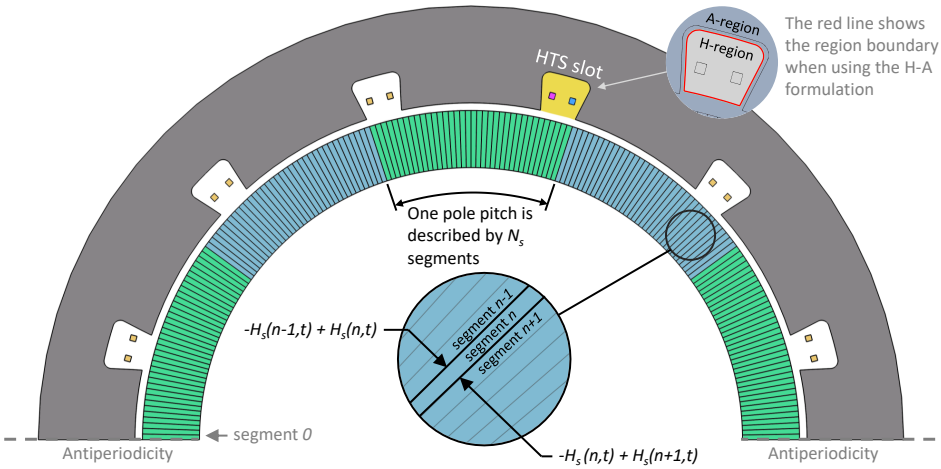

Fig. 2. Static FE model of the studied SCM. The Halbach array from Fig. 1 has been replaced with an array of small radially magnetized PM segments excited with time-varying boundary sources. The geometry is identical for the H-A and T-A formulations, with the exception that the H-A formulation requires an extra boundary line as shown top right. With this choice, the H-region only contains HTS coils and air.

TABLE I
KEY SPECIFICATIONS OF THE STUDIED SCM [17]

Description	Symbol	Value
Rated power	P	1000 kW
Nominal speed	n	3500 rpm
Electrical frequency	f	291.67 Hz
Nominal current	$\hat{I}_{ph}$	142.7 A
Number of poles	p	10
Number of phases	m	3
Number of slots	q	12
Number of turns per HTS coil	N_{HTS}	40
Active length	l_a	0.25 m
Machine diameter	D_o	0.4728 m
Mean air gap radius	R_δ	0.175 m
Air gap length	δ	4 mm

saliency can substantially impact the armature reaction, making it a crucial factor to consider. As a result, we have listed the inclusion of saliency models as a potential area for further research in Section VII.

A. Small-Segment Representation of the PMs

Fig. 2 shows how the Halbach array from Fig. 1 has been replaced with an array of small PM segments. These PM segments remain fixed throughout all time-steps of the FEA, which eliminates the need for a moving mesh.

To compensate for the absence of a moving rotor, the magnetization of each of the small PM segments must instead vary with time. By setting individual time-dependent sources on each segment, it is possible to synthesize an air gap field that moves with synchronous speed and has a spatial distribution that closely resembles that of the original Halbach array. This is achieved by applying H-fields on the segment boundaries[1], as exemplified for segment n in Fig. 2. The boundary H-fields are only applied to the radially directed boundaries since each segment shall be radially magnetized. The field applied to each of the boundaries is provided by a function H_s that depends on the segment number n (to create a spatial field distribution) and time t (to make the field move with synchronous speed ω_{el}). Since two adjacent segments share the same boundary, the source on each boundary must contain two H_s terms as shown in Fig. 2. The function H_s is given by

$$H_s(n,t) = \frac{\overbrace{B_r}^{H_c}}{\mu_r \mu_0} \cdot \cos\left(\frac{\alpha_s}{p}\right) \cdot \sum_i f_i(n,t). \tag{1}$$

In a PM, the coercive field, H_c, depends on the recoil permeability μ_r and remanent flux density B_r. Next in eq. (1), $\cos(\alpha_s/p)$ accounts for the angular span, in mechanical radians, of each of the small PM segments. The segment angle α_s is given in electrical radians by the expression

$$\alpha_s = \frac{\pi}{N_s}. \tag{2}$$

N_s is the number of segments per rotor pole.

The last part of eq. (1) is the summation of the Fourier terms which describes the velocity and shape of the rotating air gap field. In practice, this summation is only done over a selection of harmonic numbers i, as explained in Section III-B. Each term in the summation is given by

$$f_i(n,t) = a_i \cdot \sin\left(i \cdot \left[\omega t + (n+0.5)\alpha_s + \theta_0\right]\right). \tag{3}$$

Here, i is the space-harmonic number, and a_i is the corresponding Fourier coefficient, which will be determined by a simple manual tuning procedure explained in Section III-C. θ_0 is an angular offset used to position the rotor field's q-axis relative to the armature field.

[1]It is also possible to use other magnetization models, such as remanent flux density. In that case, the source shall be applied to the segment surfaces and not the boundaries.

B. Analysis of the Air Gap Field From the Halbach Array

To be able to determine the coefficients a_i in eq. (3), it is first necessary to perform an analysis of the air gap flux density $B_\delta(\theta)$ produced by the actual Halbach configuration in the studied SCM (Fig. 1). To exclude the influence from slots and armature reaction from this analysis, the model shall have a completely smooth stator surface and no armature conductors, as depicted in *Step 1* in Fig. 3-A. This model is used to establish the radial flux density distribution produced from the Halbach array, $B_\delta(\theta)$, as a function of position θ along the circumference at mean air gap radius, R_δ, as depicted in *Step 2* in Fig. 3-A. The Fourier coefficients b_i of $B_\delta(\theta)$ can now be found by applying the Euler formula on $B_\delta(\theta)$, yielding

$$b_i = \frac{p}{2\pi} \int_0^{2\pi/p} B_\delta(\theta) \cdot \sin\left(i \cdot \frac{p}{2}\theta\right) \, d\theta. \tag{4}$$

Since this representation only contains the sine term it applies to signals with odd symmetry around $\theta = 0$. When performing the harmonic analysis the rotor must therefore be positioned such that the flux density distribution has a zero-crossing at $\theta = 0$. From this analysis, only the dominant coefficients b_i found from eq. (4) are selected, as illustrated in *Step 3* in Fig. 3-A. This is done to avoid including negligible Fourier terms in the small-segment representation.

C. Synthesizing the Air Gap Field With Small Segments

The Fourier coefficients, b_i, found from eq. (4) will now be used to synthesize an approximation, B'_δ, of the air gap field from the actual PMs, B_δ, by means of the small-segment representation. The smooth-stator FE model in *Step 4* in Fig. 3-B is used for this purpose. The process of synthesizing the air gap field consists of tuning the a_i coefficient values in eq. (3). It is most conveniently done by first setting a_i equal to the Fourier coefficients b_i from eq. (4) as an initial guess[2]. Then, one coefficient a_i is tuned at a time by setting the remaining coefficients to zero. For each coefficient, the tuning-process involves three steps.

(i) Solve the smooth-stator model in Fig. 3-B with the initial guess for coefficient $a_{i,0} = b_i$ and read out the resulting peak value, $b'_{i,0}$, of the air gap field for the i^{th} harmonic.

(ii) This peak value is now used to scale the initial guess for $a_{i,0}$, such that the final value becomes

$$a_i = a_{i,0} \cdot \frac{b_i}{b'_{i,0}}. \tag{5}$$

(iii) Solve the problem again with the updated a_i from eq. (5) and confirm that the resulting peak-value of the air gap harmonic b'_i is identical to that of the Halbach array, b_i. If necessary, repeat steps (ii) and (iii).

After each coefficient, a_i, has been tuned in this way, one ends up with a set of air gap Fourier components, b'_i, identical to those produced from the Halbach array, b_i (*Step 5* vs. *Step 3* in Fig. 3). The obtained coefficients, a_i, will now be used in eq. (3) to synthesize the air gap flux density B'_δ, as depicted in *Step 6* in Fig. 3-B.

[2]Notice the principal difference between a_i and b_i. The former is related to the small-segment excitation, whereas the latter relates to the observed flux density in the air gap. Setting them equal as an initial guess is just a pragmatic approach.

IV. Application of Methodology

This section details the application of the small-segment representation to the studied SCM in Fig. 1. Other relevant model implementation details are also given herein.

A. The H-A and T-A Formulations

The studied SCM has been modeled using both the H-A and the T-A formulations to provide a broader basis for assessing the speed and accuracy of the small-segment approach. Both formulations are described in the literature. For the H-A formulation, the methodology of Brambilla *et al.* [1] has been applied, whereas the T-A implementation follows the methodology of Liang *et al.* [2].

For both the H-A and T-A formulations, the rotor PMs are located in the purely A-formulated region. There is, therefore, no principal difference between the two formulations in how the small-segment representation is implemented.

B. Small-Segment Implementation

First, the smooth stator model with Halbach array in Fig. 3-A has been analyzed to obtain the air gap flux density distribution generated from the actual PMs. When applying the Euler formula from eq. (4) on the radial flux density distribution $B_\delta(\theta)$ we find that there are three dominant space-harmonics, i.e., the 1st, 9th and 17th. Table II lists the obtained coefficient values[3].

TABLE II
Air gap Fourier coefficients from the Halbach array field

		Value	
Description	Coefficient	H-A	T-A
Fundamental	b_1	1.0387	1.0015
9th harmonic	b_9	-0.0906	-0.0907
17th harmonic	b_{17}	0.0257	0.0261

The number of small segments per pole, N_s, determines the resolution of each space-harmonic. Special attention must be paid to the highest harmonic, the 17th harmonic, since it will have the fewest segments representing one wavelength and, therefore, the lowest resolution. In our case, we take into account that the amplitude of the 17th harmonic is small, so it is tolerable that this is represented by relatively few segments. $N_s = 36$ is chosen, yielding 2.12 segments per half-wave for the 17th harmonic and 4 segments per half-wave for the 9th harmonic. After tuning the excitation of the small segments according to the procedure described in Section III-C and Fig. 3-B, we end up with the coefficients a_i listed in Table III.

[3]There is a small discrepancy between coefficients obtained for the H-A and T-A formulated models. The SCMs are identical, but the arbitrary Lagrangian-Eulerian (ALE) method [1], which is only used in the H-A formulated model, seems to produce slightly inaccurate results. For consistency, these results will also be used in the small-segment model. Hence there are two sets of coefficient values in Table II.

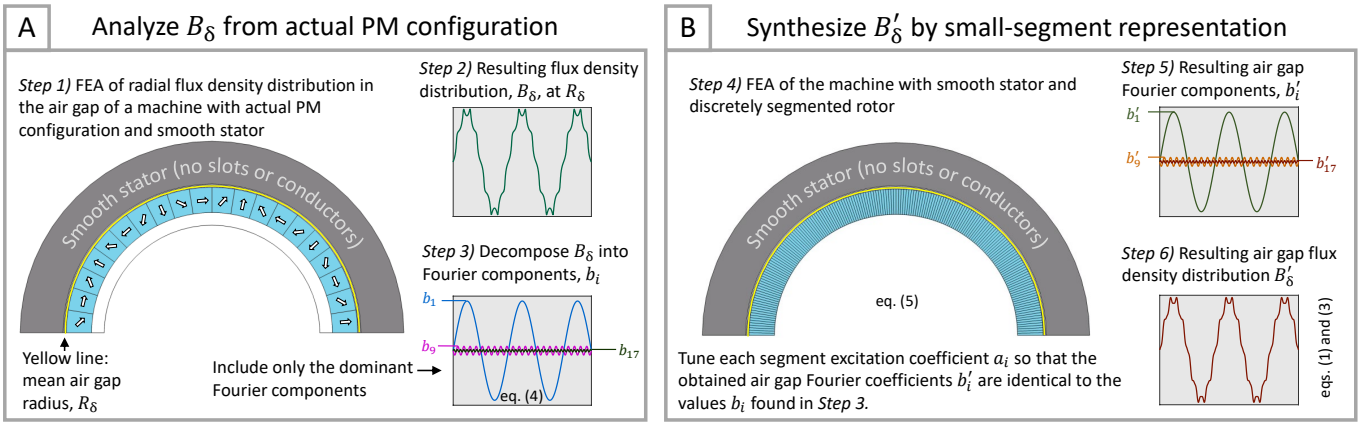

Fig. 3. The steps involved in (A) analyzing the radial flux density distribution, B_δ, produced by the Halbach array, and (B) using small segments to create a synthesized version, B'_δ, of B_δ.

TABLE III
FOURIER COEFFICIENTS IN EQ. (3) FOR THE SMALL-SEGMENT ARRAY

Description	Coefficient	Value H-A	Value T-A
Fundamental	a_1	1.2480	1.2034
9th harmonic	a_9	−0.2280	−0.2279
17th harmonic	a_{17}	0.1216	0.1234

The tuning only requires analyzing a single rotor position on a model without slots or coils. It took less than 15 minutes to tune each of the H-A and T-A formulated models.

Fig. 4 compares the radial flux density distribution from the Halbach array with that of the small-segment array. The maximum observed absolute difference between the two curves is $22.6\,\mathrm{mT}$ for the H-A formulation (not shown) and $26.2\,\mathrm{mT}$ for the T-A formulation (shown in Fig. 4).

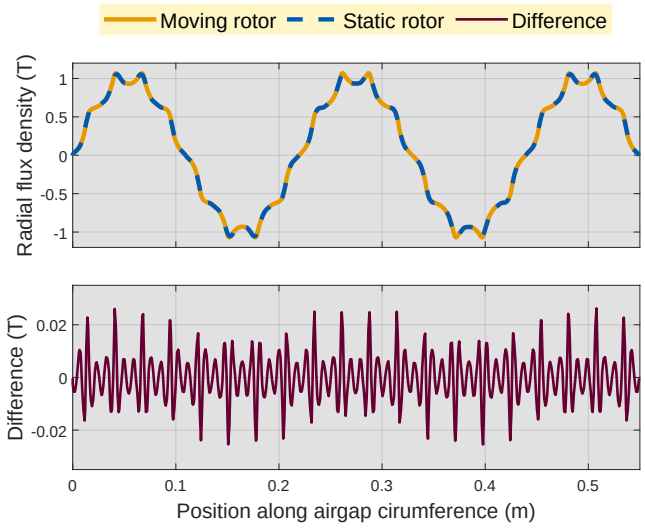

Fig. 4. Radial flux density distribution in the air gap of the example-SCM for the T-A formulation with smooth stator. The upper graph compares the flux density distribution produced by the moving rotor (Halbach array) to the same distribution produced by the static rotor (small segments). The lower graph shows the difference between the two.

C. HTS Coil Representation

For the majority of the models analyzed in this study, the HTS coil-sides are modeled as homogenized cross-sections, following the methods in [18] for the H-formulation, and [19] for the T-A formulations. The homogenized HTS coil models used here only take into account the superconducting layers of the HTS strips, leaving out the influence of the other layers in the strips (copper, silver, substrate, and so on). In addition, the coils are effectively modeled as series-wound in the homogenized representation. The HTS coil dimensions and element resolution are shown in Fig. 7.

For completeness, we have also carried out FEA on an additional set of selected cases where each turn of the coil is modeled explicitly, with results reported in Section VI.

To reduce computation time, only one slot contains representative HTS models, as shown in Fig. 2. The remaining five slots contain lossless conductors modeled in the A-formulation. As indicated by the *alternative anti-symmetry line* in Fig. 1, any coil-side pair can be placed in the HTS slot by shifting the winding layout in the model the desired number of steps in the clockwise or counter-clockwise direction. This shift is achieved by redefining the current sources for each of the conductor cross-sections and adjusting the rotor offset by changing θ_0 in eq. (3).

D. HTS Material Representation

An HTS from Shanghai Superconductor was chosen for the studied SCM. Its material characteristics [20] are comprehensively documented in the Robinson HTS Wire Critical Current Database, available online [21]. $60\,\mathrm{K}$ has been chosen as the operating temperature. The critical current at self-field is $1472\,\mathrm{A/cm}$ at this temperature, which yields $I_{c(s.f.)} = 442$ A for the $3\,\mathrm{mm}$ wide HTS tapes used in the studied SCM. Nominal phase current is thus reached at $\hat{I}_{\mathrm{ph}} = 0.32 \cdot I_{c(s.f.)}$.

Anisotropic, Kim-like [22] models are used for the magnetic field dependency of the critical current parameter J_c and the power-law index n in the E-J power-law [5], yielding

$$\rho_{HTS} = \frac{E_c}{J_c(\mathbf{B}_{ext})} \left(\frac{|J|}{J_c(\mathbf{B}_{ext})} \right)^{n(\mathbf{B}_{ext})-1} . \qquad (6)$$

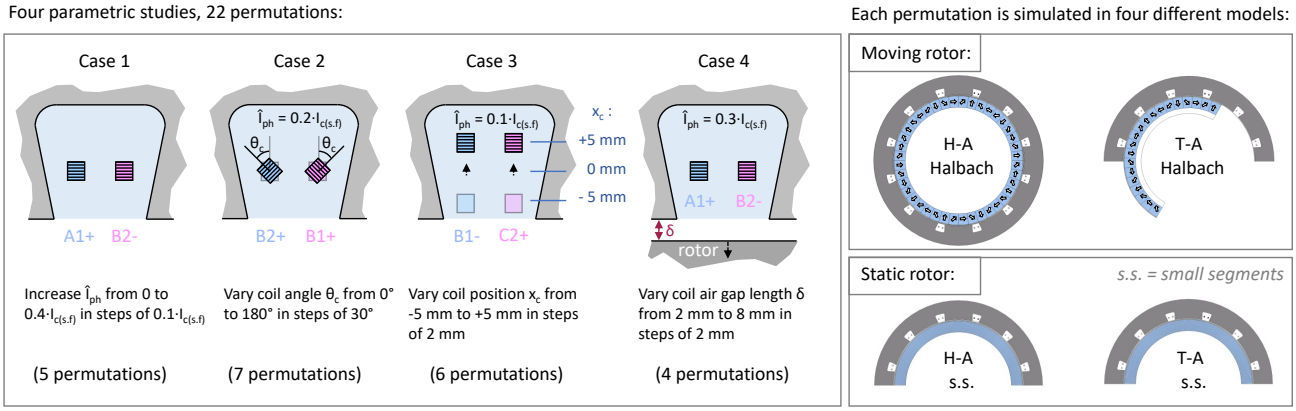

Fig. 5. Overview of parametric studies. Cases 1-4 yield 22 permutations, and each permutation has been analyzed for FEA models with moving Halbach rotors as well as static rotors with small PM segments. Each of these models have been analyzed using both the H-A and T-A formulations. Hence, a total of (5+7+6+4) × 4 = 88 simulations have been conducted.

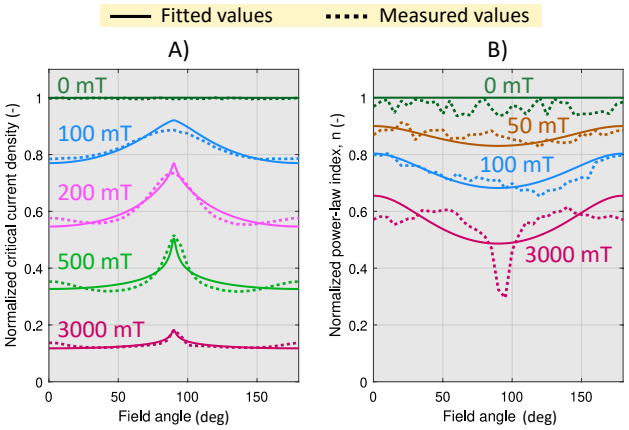

Fig. 6. Fitted values for (A) the normalized critical current density J_c and (B) the power-law index n shown for a selection of B_{ext} values. The measured values are obtained from [20] and apply to operation at 60 K.

In this work, models from [23] and [24] have been used to model the critical current density's dependence on the magnitude and angle of the external field $\mathbf{B}_{ext}$. Fig. 6-A plots the Shanghai Superconductor data fitted to these models. A model on the same form as [23] has also been used for the power-law index n. The fitted data are plotted in Fig. 6-B.

V. Comparison of Results From Small-Segment Models vs. Conventional Halbach Models

The objective of this section is to compare the performance of the FEA models based on small segments to the results obtained when the rotor is conventionally modeled as a moving Halbach array. This is done by performing three parametric studies where the results are compared for all parameter permutations. Since HTS loss is a key design parameter, we will compare the average loss Q in the HTS coil-sides, where

$$Q = \frac{2}{T_{el}} \int_{t_0}^{t_0+T_{el}/2} \dot{Q}(t)\, dt. \tag{7}$$

The integration is performed over the second half-wave, starting at $t = t_0$, of the integrand when Q has reached its steady-state value. $\dot{Q}(t)$ is the instantaneous loss per meter integrated over the HTS cross-section, given by

$$\dot{Q}(t) = \iint_{S_{HTS}} \mathbf{E}(t) \cdot \mathbf{J}(t) dS. \tag{8}$$

In addition to comparing these average values, the instantaneous curve-shape of $\dot{Q}(t)$ is also compared directly to check that the results from the small-segment model corresponds well with the results from the Halbach model. A similar assessment is also done to compare the shape of the air gap flux density distribution produced by the two representations.

A. Simulation Cases

Fig. 5 depicts the scope of the parametric study, where four different cases are investigated. The simulation cases and permutations are listed in Table IV. In Case 1, the upper value for the phase current is set to $\hat{I}_{ph} = 0.4 \cdot I_{c(s.f.)}$ since parts of the HTS coil are near current saturation at this value (cf. Fig. 6). In Case 2, the coil-sides are rotated in opposite directions from 0° to 180° in incremental steps of 30° while the phase current is kept constant at $\hat{I}_{ph} = 0.2 \cdot I_{c(s.f.)}$. In Case 3, the coil-sides are moved laterally in the radial direction, starting with an offset of $-5\,\mathrm{mm}$ ($2\,\mathrm{mm}$ removed from the air gap) and then moved a total distance of $10\,\mathrm{mm}$ toward the outer slot radius in $2\,\mathrm{mm}$ steps while the phase current is kept constant at $\hat{I}_{ph} = 0.1 \cdot I_{c(s.f.)}$. For this case we chose a relatively low $\hat{I}_{ph}$ value to ensure that the magnetizing losses arising from the exposure to the rotor field will constitute a significant proportion of the total losses in the HTS coil-sides. In case 4, the effect of the air gap length is investigated by varying δ from $2\,\mathrm{mm}$ to $8\,\mathrm{mm}$ at $\hat{I}_{ph} = 0.3 \cdot I_{c(s.f.)}$.

Different slots are analyzed for the four cases since the coil-sides in the slots are subjected to different conditions depending on the phase and polarity of their neighboring coil-side. The coil-sides' phases and polarities are shown in Fig. 5. These combinations effectively represent all the other phase-combinations in the SCM's 12 slots. Both the H-A and the T-A formulations have been employed in the parametric studies. The studied SCM has been modeled with moving Halbach

TABLE IV
SIMULATION CASES AND PERMUTATIONS FOR PARAMETRIC STUDIES

	Description	Lower value	Upper value	Number of steps
Case 1	Phase current ($\hat{I}_{ph}$)	0 A	$0.4 \cdot I_{c(s.f.)}$	5
Case 2	Coil angle (θ_c)	0°	+180°	7
Case 3	Coil position (x_c)	-5 mm	+5 mm	6
Case 4	Air gap length (δ)	2 mm	8 mm	4

arrays and static small-segment arrays for both formulations. Notice that with the H-A formulated Halbach model, it has not been possible to utilize the anti-symmetry of the studied SCM. This will yield comparatively longer computation times for this model.

B. Mesh and Solver Settings

The mesh resolution is identical for all models, with two exceptions. The PMs are fundamentally different for the small-segment representation (Fig. 7) and the Halbach array (Fig. 1), and, consequently, the mesh must be different. The Halbach rotor is coarsely meshed. The other difference is that the H-A formulation uses a boundary between the H- and A-formulated regions [1], cf. Fig. 2. This adds some extra elements to the H-A-formulated models.

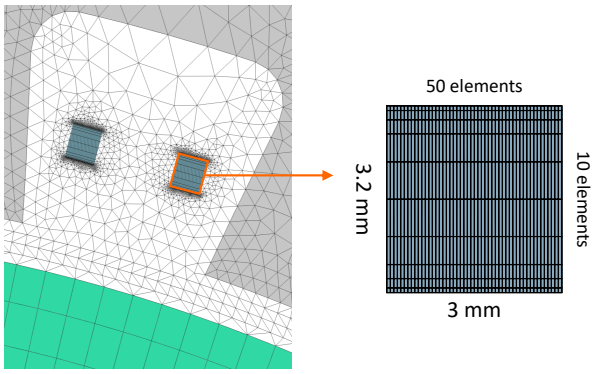

Fig. 7. Model mesh. Both the HTS coils and the PM segments are modeled with rectangular elements.

The solver settings have been set equal for all models, with the two exceptions listed in Table V.

TABLE V
DISSIMILARITIES IN FEA SOLVER SETTINGS

	Halbach rotor, moving		Small segments, static	
	H-A	T-A	H-A	T-A
Solver	MUMPS	MUMPS	MUMPS	PARDISO
Jacobian update	Minimal	Every iteration	Minimal	Minimal

The T-A-formulated Halbach model had to be run with more frequent Jacobian updates to prevent convergence problems[4]. The computation speed of the T-A formulated small-segment model increased with the PARDISO solver, so this was used since there were no convergence issues.

[4]The T-A-formulated model with Halbach rotor still failed to converge for one of the 22 parameter permutations, see Section V-E.

C. Computational Resources

The simulations were carried out on the IDUN cluster [16] at the Norwegian University of Science and Technology (NTNU). 16 batch jobs were executed in total. Each batch constituted one case and one model from Fig. 5.

Measures have been taken to ensure that equal computing resources are allocated to all batch runs. These include reserving exclusive access to all computing nodes and only selecting nodes from servers of the same model (Dell Poweredge C6420). There are, however, some variations in the number of CPUs and cores, as well as memory size, which affect the performance. We have carefully inspected the node assignments for each job, and there is no indication of any systematic bias that would significantly benefit any of the batch jobs over the others in terms of computing times. Consequently, we can expect consistency when we compare the computing times of the different models and formulations.

D. Errors

The reader is referred to Appendix A for a complete overview of the obtained results. When assessing errors, the results produced from models with moving Halbach rotors are taken as reference values.

The accuracy of the losses estimated from the static rotor models is evaluated by two different metrics. The first is the relative error in the average coil-loss calculated from eq. (7). The largest relative error observed in this study was for Case 1 (T-A formulation) when the current is zero. In this case, the average loss calculated from the small-segment model is $4.12\,\%$ below the average loss calculated from the Halbach model. The left plot in Fig. 8 compares the shapes of the instantaneous loss curves for this permutation.

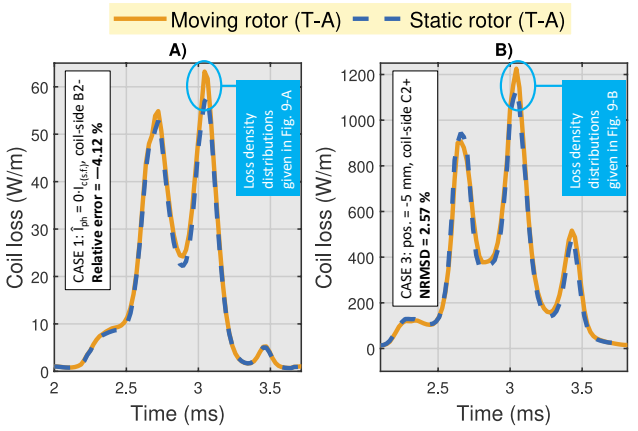

Fig. 8. Comparison of instantaneous loss for the largest relative error (A) and the largest NRMSD (B) in the parametric studies (T-A form.).

The second metric establishes the deviation in the shape of the instantaneous loss-curves over one half-period. For this purpose, the normalized root-mean-square deviation (NRMSD) is used in eq. (9), where $\dot{Q}$ is obtained from eq.

(8), and k is the time step element number with N elements in total.

$$\text{NRMSD} = \frac{\sqrt{\frac{1}{N}\sum_{k=1}^{N}\left(\dot{Q}_{ref}(t\,[k]) - \dot{Q}_{est}(t\,[k])\right)^2}}{\dot{Q}_{ref,max} - \dot{Q}_{ref,min}} \tag{9}$$

The largest deviation was observed for Case 3 (T-A formulation) when the coil position x_c was -5 mm. In this case, the deviation is 2.57 %. The comparison of curve-shapes for this permutation is shown in the right plot in Fig. 8.

Fig. 8 shows that the estimated losses with the static rotor models are very close to those calculated with a moving rotor, even for these worst-case estimates of Q and $\dot{Q}$. Fig. 9 shows the loss distribution in the windings for the same two cases as Fig. 8. The loss distribution is shown at the instance when the deviation in $\dot{Q}$ is maximum. The H-A results from the same cases are included for comparison.

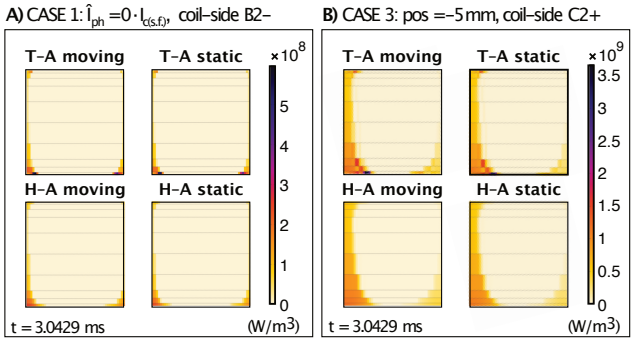

Fig. 9. Comparison of loss density distribution in the coil sides (element-wise average). The distibutions correspond to the peak losses in Fig. 8 (t=3.0429 ms). The H-A results from the same cases have been included for comparison.

In addition to assessing the loss values we have also calculated the deviation in the small-segment representation's air gap flux density distribution. The deviation is given in NRMSD, similar to eq. (9). Cases 1 and 4 produced the largest deviations, and the results are listed in Table VI.

TABLE VI
NORMALIZED ROOT-MEAN-SQUARE DEVIATION (NRMSD) OF AIR GAP FLUX DENSITY FROM CASES 1 AND 4

		Normalized current loading ($\hat{I}_{ph}/I_{c(s.f.)}$)				
Case 1		0	0.1	0.2	0.3	0.4
	H-A	0.39 %	0.61 %	0.94 %	1.24 %	1.50 %
	T-A	0.43 %	0.72 %	1.16 %	1.54 %	1.86 %
		Air gap length (δ)				
Case 4		2 mm	4 mm	6 mm	8 mm	
	H-A	1.25 %	1.25 %	1.27 %	1.26 %	
	T-A	1.50 %	1.54 %	1.57 %	1.58 %	

The results in Table VI shows that the deviation reaches 1.86 % (NRMSD) at maximum current. Still, the synthesized air gap flux corresponds well with the field from the Halbach array, as Fig. 10 shows.

In the parametric studies, the largest observed deviation in average torque was 0.64 %. The corresponding ripple torque is less accurately captured by the small-segment model. Here,

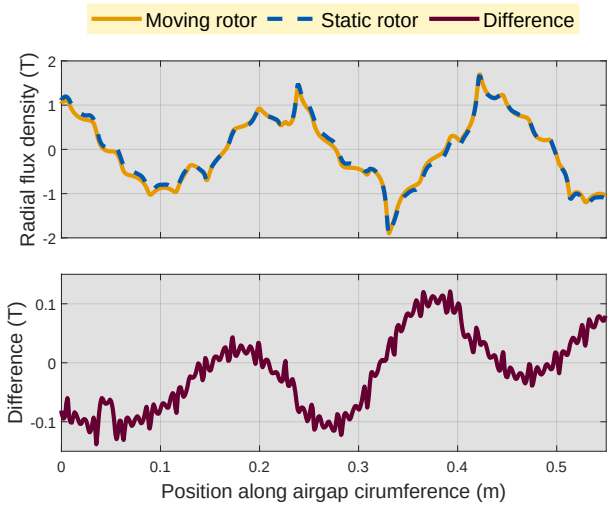

Fig. 10. Radial flux density distribution in the air gap of the studied SCM. The results are from Case 1 at the instance of peak current in phase A (T-A formulation, $\hat{I}_{ph} = 0.4 \cdot I_{c(s.f.)}$).

deviations as high as 92 % were observed, but this must be seen in conjunction with the small ripple values (1.15 % in the Halbach model and 0.09 % in the corresponding small-segment model for the worst case with 92 % deviation).

E. Computation Times

The T-A formulated Halbach model failed to converge for pos. = −1 mm in Case 3 (cf. Table XII). To preserve consistency, the results from this permutation have been excluded for all models and formulations when evaluating the computation times. Table VII lists the aggregated computation times for Cases 1-4. Also listed are the total computation times and the corresponding speedup factors which are measures of the gain in computation speed when using the small-segment representation instead of the full Halbach models.

TABLE VII
COMPUTATION TIMES FROM THE PARAMETRIC STUDY OF THE STUDIED SCM WITH HOMOGENIZED COIL MODELS

	Halbach rotor, moving		Small segments, static	
	H-A	T-A	H-A	T-A
Case 1	21 h 15 min	17 h 45 min	1 h 23 min	0 h 28 min
Case 2	29 h 32 min	22 h 9 min	1 h 43 min	0 h 39 min
Case 3	22 h 22 min	18 h 58 min	1 h 6 min	0 h 25 min
Case 4	15 h 26 min	12 h 28 m	1 h 1 min	0 h 21 min
Total	88 h 35 min	71 h 20 min	5 h 13 min	1 h 53 min
Speedup	-	-	17.0x	37.9x

The gain in speed is significant, especially for the T-A formulation where the increased numerical stability of the small segment model also allows us to use the PARDISO solver (cf. Table V) which in this case is faster than the MUMPS solver.

VI. COMPARISON OF RESULTS FROM MORE DETAILED COIL MODELS

The results evaluated thus far have been based on homogenized HTS coil models [18], [19]. Here, we will briefly investigate the performance of the small-segment representation

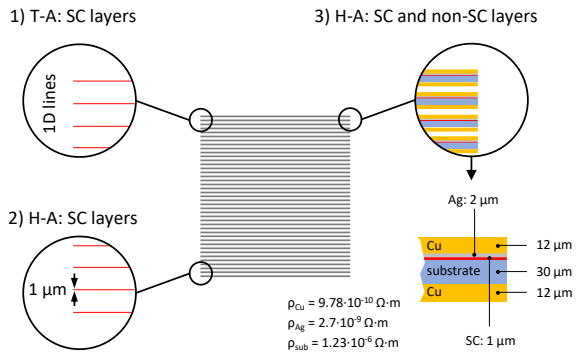

Fig. 11. Three different approaches to explicit coil modeling in the example-SCM. In models 1 and 2 only the HTS strips' SC layers are modeled. In model 3, the non-superconducting layers (copper, silver and Hastelloy substrate) are also included. The layer thicknesses have been set notionally and are not representative of a specific product. The SC layer is modeled as previously (Fig. 6). The remaining conditions are identical to Case 2 with $\theta_c = 0°$ (cf. Fig. 5 and Table XI).

when the HTS coil models contain more details, as shown in Fig. 11. Each of the coil's 40 turns is explicitly modeled, and the level of detail in the coil cross-section varies. In model 1 (T-A) and 2 (H-A) only the superconducting layers are included, whereas model 3 (H-A) also includes the copper, silver and substrate layers.

Like before, the simulations were run on computing nodes with identical performance. The solver settings were identical to what was used previously (Table V), except this time also the T-A formulated model was run with minimal Jacobian update since this did not cause convergence issues. There were 66 elements across each cross-section of the HTS strip. The results are summarized in Tables VIII and IX.

TABLE VIII
HTS COIL LOSS PRECISION FOR THE STUDIED SCM WITH EXPLICIT COIL MODELS

	SC layers only				All layers	
	T-A		H-A		H-A	
	B2+	B1+	B2+	B1+	B2+	B1+
Moving rotor (W/m)	139.6	205.3	148.0	208.2	146.4	206.4
Static rotor (W/m)	138.7	201.8	144.2	209.8	142.4	207.7
Relative error (%)	-0.64	-1.70	-2.57	0.77	-2.73	0.63
NRMSD (%)	0.56	1.01	1.44	0.33	1.49	0.34

TABLE IX
COMPUTATIONAL TIMES OF THE STUDIED SCM WITH EXPLICIT COIL MODELS

	SC layers only		All layers
	T-A	H-A	H-A
Moving rotor	5h 12m	11h 1m	31h 11m
Static rotor	8m 30s	45m 43s	3h 15m
Speedup factor	36.7x	14.5x	9.6x

The results in Tables VIII and IX show that the small-segment representation performs very well with more detailed coil models as well. Overall, the errors and speedup factors are comparable to those obtained with the homogenized models. In the case where all layers were explicitly modeled (model 3 in Fig. 11), the speedup factor drops to 9.6x. This can probably be attributed to the high level of detail in the HTS coil model. With this level of detail, the coil models constitute a larger proportion of the total SCM model. Still, the observed tenfold increase in computation speed compared to the Halbach model represents a remarkable improvement.

VII. Conclusion

This paper has shown how the proposed small-segment static rotor representation can reduce FEA computation times by more than an order of magnitude for AC SCMs with HTS stator windings and surface-mounted PM rotors. The parametric case studies were conducted on a rotor with Halbach configuration, but the method is generally applicable to surface-mounted PM configurations. The parametric studies achieved gross speedup factors of 17.0x for H-A-formulated models and 37.9x for T-A-formulated models. This comes at the cost of slightly reduced accuracy in the HTS loss calculations. The highest relative error in the average coil loss was $4.12\,\%$, while the maximum deviation (NRMSD) in the curve-shape of the instantaneous loss was $2.57\,\%$.

The actual rotating PM geometry is sacrificed with the small-segment static representation. It is, therefore, not suitable for analyzing rotor phenomena such as PM loss or PM operation points. Hence, the method is mainly aimed at performing studies of HTS stator phenomena and optimization. Since the air gap flux density is accurately approximated, the small-segment representation will also yield reasonable estimates for the torque produced in the SCM.

One limitation of this paper is that only 2D models have been considered. However, there should be no principal difference in applying the method to 3D models where the reduction in model complexity can potentially have even more impact. Although the method has been investigated in conjunction with HTS armature coils, it is not limited to any specific conductor materials. However, other methods [11], [12] can be more efficient for analyzing conventional conductors. In a future research item, it should be investigated whether the small-segment static rotor representation can be applied successfully to SCM topologies with other rotor configurations, such as iron-less rotors with superconducting magnetizing coils and, potentially, static representations of rotating magnetic saliency.

Appendix A
Detailed Simulation Results

Tables X-XII list the detailed results from Cases 1 to 4. The maximum values for the relative error and NRMSD are listed in bold writing for each simulation case. The T-A-formulated Halbach model failed to converge for a coil offset of $-1\,\mathrm{mm}$ in Case 3, so these entries are left blank in Table XII.

Acknowledgment

The authors want to thank A. Gytri at NTNU for his valuable help with setting up the IDUN calculations. We would also like to thank the initiators of, and contributors to, the Robinson HTS Wire Critical Current Database [21], and the HTS Modeling Workgroup [25].

TABLE X
DETAILED HTS LOSS RESULTS FOR CASE 1, INCLUDING RELATIVE ERROR AND NORMALIZED ROOT-MEAN-SQUARE DEVIATION (NRMSD)

	Phase current →	$\hat{I}_{ph} = 0 \cdot I_{c(s.f.)}$		$\hat{I}_{ph} = 0.1 \cdot I_{c(s.f.)}$		$\hat{I}_{ph} = 0.2 \cdot I_{c(s.f.)}$		$\hat{I}_{ph} = 0.3 \cdot I_{c(s.f.)}$		$\hat{I}_{ph} = 0.4 \cdot I_{c(s.f.)}$	
	Coil-side ID →	A1+	B2-	A1+	B2-	A1+	B2-	A1+	B2-	A1+	B2-
H-A	Moving rotor (W/m)	14.8	15.2	32.5	59.4	136.4	223.3	487.6	675.7	1548.1	1852.3
	Static rotor (W/m)	14.5	14.8	32.4	58.1	136.6	218.7	487.8	663.9	1546.2	1830.3
	Relative error (%)	-2.03	-2.63	-0.31	-2.19	0.15	-2.06	0.04	-1.75	-0.12	-1.19
	NRMSD (%)	1.54	1.49	1.39	1.49	1.21	1.68	1.08	1.57	0.88	1.13
T-A	Moving rotor (W/m)	16.2	17.0	33.4	63.8	137.6	227.7	491.8	682.5	1553.6	1864.9
	Static rotor (W/m)	15.6	16.3	33.0	61.4	137.0	221.2	488.9	664.4	1542.8	1824.7
	Relative error (%)	-3.70	**-4.12**	-1.20	-3.76	-0.44	-2.85	-0.59	-2.65	-0.70	-2.16
	NRMSD (%)	2.31	2.20	1.57	**2.40**	1.48	2.05	1.39	1.88	1.06	1.38

TABLE XI
DETAILED HTS LOSS RESULTS FOR CASE 2, INCLUDING RELATIVE ERROR AND NORMALIZED ROOT-MEAN-SQUARE DEVIATION (NRMSD)

	Coil rotation →	$\theta_c = 0°$		$\theta_c = 30°$		$\theta_c = 60°$		$\theta_c = 90°$		$\theta_c = 120°$		$\theta_c = 150°$		$\theta_c = 180°$	
	Coil-side ID →	B2+	B1+	B2+	B1+	B2+	B1+	B2+	B1+	B2+	B1+	B2+	B1+	B2+	B1+
H-A	Moving rotor (W/m)	146.0	219.1	571.2	126.7	936.5	93.4	873.5	149.7	473.7	238.0	113.8	275.8	145.9	219.4
	Static rotor (W/m)	144.9	216.3	565.9	125.1	928.2	93.7	867.0	150.5	470.8	238.0	114.1	273.3	145.0	216.3
	Relative error (%)	-0.75	-1.28	-0.93	-1.26	-0.89	0.32	-0.74	0.53	-0.61	0.0	0.26	-0.91	-0.62	-1.41
	NRMSD (%)	0.65	0.93	0.74	0.99	0.84	0.9	0.66	0.51	0.45	0.19	0.24	0.65	0.59	0.97
T-A	Moving rotor (W/m)	146.1	221.5	580.1	125.7	962.6	96.4	889.3	159.3	488.1	247.6	119.0	281.6	146.1	221.6
	Static rotor (W/m)	144.9	217.9	574.0	123.8	948.1	96.9	879.6	160.7	485.1	247.6	119.0	278.8	144.9	217.9
	Relative error (%)	-0.82	-1.63	-1.05	-1.51	-1.51	0.52	-1.09	0.88	-0.61	0.0	0.0	-0.99	-0.82	**-1.67**
	NRMSD (%)	0.63	1.11	0.79	1.11	**1.55**	0.86	0.85	0.65	0.44	0.19	0.14	0.66	0.63	1.11

TABLE XII
DETAILED HTS LOSS RESULTS FOR CASE 3, INCLUDING RELATIVE ERROR AND NORMALIZED ROOT-MEAN-SQUARE DEVIATION (NRMSD)

	Coil position →	$x_c = -5\,mm$		$x_c = -3\,mm$		$x_c = -1\,mm$		$x_c = +1\,mm$		$x_c = +3\,mm$		$x_c = +5\,mm$	
	Coil-side ID →	B1-	C2+	B1-	C2+	B1-	C2+	B1-	C2+	B1-	C2+	B1-	C2+
H-A	Moving rotor (W/m)	276.3	296.5	97.4	138.4	44.1	76.3	25.8	47.8	18.5	32.8	15.4	25.2
	Static rotor (W/m)	271.6	286.5	96.0	134.1	43.5	74.1	25.4	46.5	18.3	32.1	15.3	24.7
	Relative error (%)	-1.70	**-3.37**	-1.44	-3.11	1.36	-2.88	-1.55	-2.72	-1.08	-2.13	-0.65	-1.98
	NRMSD (%)	1.65	1.93	1.55	1.76	1.39	1.62	1.39	1.72	1.07	1.46	0.88	1.27
T-A	Moving rotor (W/m)	275.4	330.4	99.0	154.3	-	-	26.0	53.0	18.5	35.7	15.4	26.2
	Static rotor (W/m)	270.6	320.0	97.6	149.6	44.0	83.0	25.6	51.3	18.3	34.8	15.3	25.7
	Relative error (%)	-1.74	-3.15	-1.41	-3.05	-	-	-1.54	-3.21	-1.08	-2.52	-0.65	-1.91
	NRMSD (%)	1.79	**2.57**	1.64	1.93	-	-	1.73	2.23	1.44	1.56	1.11	1.22

TABLE XIII
DETAILED HTS LOSS RESULTS FOR CASE 4, INCLUDING RELATIVE ERROR AND NORMALIZED ROOT-MEAN-SQUARE DEVIATION (NRMSD)

	Air gap length →	δ = 2 mm		δ = 4 mm		δ = 6 mm		δ = 8 mm	
	Coil-side ID →	B2+	B1+	B2+	B1+	B2+	B1+	B2+	B1+
H-A	Moving rotor (W/m)	520.7	678.3	500.2	648.8	485.5	627.2	473.3	608.3
	Static rotor (W/m)	519.1	671.0	498.5	643.1	485.0	622.3	472.4	604.4
	Relative error (%)	-0.31	-1.08	-0.34	-0.88	-0.10	-0.78	-0.19	-0.64
	NRMSD (%)	0.44	0.77	0.34	0.64	0.23	0.66	0.25	0.52
T-A	Moving rotor (W/m)	516.8	674.7	500.5	648.9	488.3	629.7	477.9	612.3
	Static rotor (W/m)	514.6	665.5	499.0	641.5	487.2	623.6	476.1	607.3
	elative error (%)	-0.43	**-1.36**	-0.30	-1.14	-0.23	-0.97	-0.38	-0.82
	NRMSD (%)	0.49	**0.89**	0.37	0.75	0.27	0.68	0.27	0.58

REFERENCES

[1] R. Brambilla, F. Grilli, L. Martini, M. Bocchi, and G. Angeli, "A finite-element method framework for modeling rotating machines with superconducting windings," *IEEE Trans. Appl. Supercond.*, vol. 28, no. 5, pp. 1–11, 2018.

[2] F. Liang and et. al., "A finite element model for simulating second generation high temperature superconducting coils/stacks with large number of turns," *J. Appl. Phys.*, vol. 122, no. 4, p. 043903, 2017.

[3] S. You, S. S. Kalsi, M. D. Ainslie, R. A. Badcock, N. J. Long, and Z. Jiang, "Simulation of ac loss in the armature windings of a 100 kw all-hts motor with various (re) bco conductor considerations," *IEEE Access*, vol. 9, pp. 130 968–130 980, 2021.

[4] H. Wei, B. Shen, A. Shah, J. Yang, L. Hao, M. Tian, J. Hu, I. Patel, Y. Öztürk, and T. Coombs, "Modeling of an axial field machine (AFM) with superconducting windings," *IEEE Trans. Appl. Supercond.*, vol. 32, no. 4, pp. 1–5, 2022.

[5] J. Rhyner, "Magnetic properties and ac-losses of superconductors with power law current—voltage characteristics," *Physica C*, vol. 212, no. 3-4, pp. 292–300, 1993.

[6] F. Huber, W. Song, M. Zhang, and F. Grilli, "The ta formulation: an efficient approach to model the macroscopic electromagnetic behaviour of hts coated conductor applications," *Supercond. Sci. Technol.*, vol. 35, no. 4, p. 043003, 2022.

[7] F. Sirois and F. Grilli, "Numerical considerations about using finite-element methods to compute ac losses in hts," *IEEE Trans. Appl. Supercond.*, vol. 18, no. 3, pp. 1733–1742, 2008.

[8] S. Mu and et. al., "Calculation and comparison of hts electromagnetic characteristics with different models," *Physica C*, vol. 589, p. 1353930, 2021.

[9] M. D. Ainslie, T. J. Flack, Z. Hong, and T. A. Coombs, "Comparison of first-and second-order 2D finite element models for calculating ac loss in high temperature superconductor coated conductors," *Int. J. Comput. Math. Electr. Electron. Eng.*, vol. 30, no. 2, pp. 762–774, 2011.

[10] T. Benkel, M. Lao, Y. Liu, E. Pardo, S. Wolfstädter, T. Reis, and F. Grilli, "T–A-formulation to model electrical machines with HTS coated conductor coils," *IEEE Trans. Appl. Supercond.*, vol. 30, no. 6, pp. 1–7, 2020.

[11] A. Tessarolo, F. Agnolet, F. Luise, and M. Mezzarobba, "Use of time-harmonic finite-element analysis to compute stator winding eddy-current losses due to rotor motion in surface permanent-magnet machines," *IEEE Trans. Energy Convers.*, vol. 27, no. 3, pp. 670–679, 2012.

[12] A. Tessarolo, C. Ciriani, N. Elloumi, M. Mezzarobba, and A. Masmoudi, "Fast computation method for stator winding skin-effect additional losses in synchronous machines with open slots and arbitrary rotor geometry," *IEEE Trans. Energy Convers.*, vol. 36, no. 2, pp. 1156–1168, 2020.

[13] E. H. Brandt and M. Indenbom, "Type-II-superconductor strip with current in a perpendicular magnetic field," *Phys. Rev. B*, vol. 48, no. 17, p. 12893, 1993.

[14] D. Meeker, "Sliding band motion model for electric machines, *FEMM*," https://www.femm.info/wiki/SlidingBand, 2018.

[15] T. J. Hughes, J. A. Cottrell, and Y. Bazilevs, "Isogeometric analysis: CAD, finite elements, NURBS, exact geometry and mesh refinement," *Comput. Methods Appl. Mech. Eng.*, vol. 194, no. 39-41, pp. 4135–4195, 2005.

[16] M. Själander, M. Jahre, G. Tufte, and N. Reissmann, "Epic: An energy-efficient, high-performance gpgpu computing research infrastructure," *arXiv preprint arXiv:1912.05848*, 2019.

[17] R. Mellerud, J. Nøland, and C. Hartmann, "Preliminary design of a 2.5-mw superconducting propulsion motor for hydrogen-powered aviation," in *Proc. Int. Conf. Electr. Mach. (ICEM)*. IEEE, 2022, pp. 1404–1410.

[18] V. M. Zermeno and et. al., "Calculation of alternating current losses in stacks and coils made of second generation high temperature superconducting tapes for large scale applications," *J. Appl. Phys.*, vol. 114, no. 17, p. 173901, 2013.

[19] E. Berrospe-Juarez, V. M. Zermeño, F. Trillaud, and F. Grilli, "Real-time simulation of large-scale hts systems: Multi-scale and homogeneous models using the T–A formulation," *Supercond. Sci. Technol.*, vol. 32, no. 6, p. 065003, 2019.

[20] S. Wimbush, N. Strickland, and A. Pantoja, "Critical current characterisation of Shanghai Superconductor Low Field High Temperature 2G HTS superconducting wire," Feb. 2022. [Online]. Available: https://figshare.com/articles/dataset/Critical_current_characterisation_of_Shanghai_Superconductor_Low_Field_High_Temperature_2G_HTS_superconducting_wire/19185092

[21] "Robinson hts wire critical current database," htsdb.wimbush.eu, accessed: 2022-11-03.

[22] Y. Kim, C. Hempstead, and A. Strnad, "Critical persistent currents in hard superconductors," *Phys. Rev. Lett.*, vol. 9, no. 7, p. 306, 1962.

[23] K. P. Thakur and et. al., "Frequency-dependent critical current and transport ac loss of superconductor strip and roebel cable," *Supercond. Sci. Technol.*, vol. 24, no. 6, p. 065024, 2011.

[24] X. Zhang, Z. Zhong, J. Geng, B. Shen, J. Ma, C. Li, H. Zhang, Q. Dong, and T. Coombs, "Study of critical current and n-values of 2g hts tapes: Their magnetic field-angular dependence," *J. Supercond. Novel Magn.*, vol. 31, no. 12, pp. 3847–3854, 2018.

[25] "Hts modeling workgroup," www.htsmodelling.com/, accessed: 2022-11-10.

Christian Hartmann received the M.Sc. degree in electric power engineering from the Norwegian University of Science and Technology (NTNU), Trondheim, Norway, in 1999. He is a Senior Researcher with the Institute for Energy Technology, and is currently pursuing a Ph.D. degree focusing on cryo-electric propulsion systems for next-generation aviation.

Runar Mellerud received his M.Sc. degree in electric power engineering at NTNU in 2021, where he is currently pursuing a Ph.D. degree in superconducting electrical machines for aerospace applications.

Jonas Kristiansen Nøland (S'14-M'17-SM'22) was born in Drammen, Norway, in 1988. He received the M.Sc. degree in electric power engineering from the Chalmers University of Technology, Gothenburg, Sweden, in 2013, and the Ph.D. degree in engineering physics from Uppsala University, Uppsala, Sweden, in 2017. Since 2018, he has been an Associate Professor with the Department of Electric Power Engineering, Norwegian University of Science and Technology. His current research interests include excitation systems, improved utilization of electrical machines, high-power machinery for aircraft applications, and transportation electrification in general. Dr. Nøland serves as an Associate Editor for the IEEE TRANSACTIONS ON ENERGY CONVERSION and the IEEE TRANSACTIONS ON INDUSTRIAL ELECTRONICS.

Robert Nilssen received his Dr.ing. degree in 1989 from the Norwegian Institute of Technology (NTH). From 1989 to 1996 Nilssen worked at NTH as associated professor. In this period he was scientific advisor for SINTEF. Since 1996 Nilssen has been a professor at the Norwegian University of Science and Technology (NTNU) - with numerical electromagnetic field calculations as his main responsibility. In this period Nilssen has participated in a series of research projects in which design and optimization has been important. Nilssen has also been co-founder of several industry companies. He has been scientific advisor for several companies and in particular for SmartMotor AS and Rolls-Royce Norway - focusing on applications of Permanent Magnet Machines.